High-order harmonic propagation in gases within the discrete dipole approximation

C. Hernández-García,[1] J. A. Pérez-Hernández,[1] J. Ramos,[1] E. Conejero Jarque,[1] L. Roso,[2] and L. Plaja[1]
[1]*Departamento de Física Aplicada, Universidad de Salamanca, E-37008 Salamanca, Spain*
[2]*Centro de Láseres Pulsados CLPU, E-37008 Salamanca, Spain*
(Received 6 July 2010; published 27 September 2010)

We present an efficient approach for computing high-order harmonic propagation based on the discrete dipole approximation. In contrast with other approaches, our strategy is based on computing the total field as the superposition of the driving field with the field radiated by the elemental emitters of the sample. In this way we avoid the numerical integration of the wave equation, as Maxwell's equations have an analytical solution for an elementary (pointlike) emitter. The present strategy is valid for low-pressure gases interacting with strong fields near the saturation threshold (i.e., partially ionized), which is a common situation in the experiments of high-order harmonic generation. We use this tool to study the dependence of phase matching of high-order harmonics with the relative position between the beam focus and the gas jet.

DOI: 10.1103/PhysRevA.82.033432 PACS number(s): 42.65.Ky

The dynamics of matter subjected to strong laser radiation departs substantially from the perturbative expectations. As a result several nonlinear phenomena appear in this regime of extreme interactions. Among them, high-order harmonic generation is possibly the most relevant, due to its potential applications. Although the detailed response of a single atom or molecule to an intense electromagnetic field is quite complex, the fundamental underlying physics can be unexpectedly simple. For the case of harmonic generation, the most relevant mechanism can be described in terms of a three-step process in which a bound electron is ionized, accelerated by the field, and finally driven back to the parent ion [1,2]. The harmonics are emitted by the rapid oscillations of the dipole induced by the continuum and the bound state. This process is responsible of the characteristic plateau structure of the harmonic spectrum, where high harmonics are radiated at similar intensities until a cutoff frequency is reached. This feature is useful for developing sources of high-frequency (xuv) coherent radiation (which may extend to the water window [3,4]). In addition, the natural phase locking of the highest frequency harmonics permits the Fourier synthesis of x-ray pulses with durations below 100 as [5]. High-order harmonics by themselves contain information of the subfemtosecond dynamics of the atomic electrons, reflecting quantum path interferences [6], or molecule dissociation dynamics and structure [7,8]. The proper theoretical description of experiments involving high-order harmonic generation has to include a faithful reproduction of not only the single radiator (atom or molecule) spectrum but also the propagation of the harmonics in the medium and its far field distribution at the detectors. The fundamental aspects for the computations of the high-order harmonic propagation were discussed by L'Huillier *et al.* in two seminal articles [9,10]. The phase matching of high-order harmonics is shown to depend on the different parameters of the experiment (including atomic species, beam shape, etc.); therefore it offers new degrees of freedom for the optimization of the harmonic yield. However, the exact computation of the propagation equations is a formidable task due to the disparity of the scales involved (few tens of nanometers for the wavelengths of the highest harmonics and propagation distances of few millimeters). In this article we propose a technique for the computation of the high-order harmonic propagation. Our method relies on the fundamental description of electric-field propagation as a superposition of the individual fields generated at different points of the target. This viewpoint is the natural starting point if one considers the integral solution of the wave equation, instead of its differential form. Maxwell equations can be integrated analytically for a pointlike source in vacuum. We shall, therefore, use this solution with the assumption that the high-order harmonics are weakly perturbed as they propagate through the medium. As we shall see in this article, this is a reasonable assumption in partially ionized low-pressure gases. By construction, our method does not resort to the usual approximations, in particular, paraxial or field envelope approximations, although these are correct assumptions in a typical experiment of high-order harmonic generation in low-pressure gases. To circumvent the problem of computing the vast quantity of elementary emitters in the target, we use the discrete dipole approximation (DDA) [11,12]. In this context, the target is assumed to be composed of a set of finite-size spheres involving a large number of elementary radiators each. The computation of harmonic propagation inside each sphere is straightforward if the incident field is assumed to be locally a plane wave.

The paper is organized in two sections. The first one describes the theoretical approach used in this article. It is divided into three subsections: First, we analyze the main approximations involving the field generation and the field propagation; second, we consider the extension of the strong-field approximation (SFA+) model approach for the evaluation of the source term [13]; and, finally, we describe the basis of our propagation model based on the DDA. In the second section we analyze the convergence of our method, showing different results at different stages of the calculation. Finally, in the third section we consider a particular case and compare our results with previous works [14,15]. The article ends with a discussion of the results in terms of the spatial phase distributions of harmonic generation.

I. THEORETICAL APPROACH

The general problem of propagation amounts to solving the wave equation for the electric field $\mathbf{E}$

$$\nabla^2\mathbf{E} - \frac{1}{c^2}\frac{\partial}{\partial t^2}\mathbf{E} = \frac{4\pi}{c^2}\frac{\partial}{\partial t}\mathbf{J}, \tag{1}$$

where $\mathbf{J}$ is the current density. Instead of solving this equation numerically, we consider its integral solution [16]: $\mathbf{E}(\mathbf{r},t) = \mathbf{E}_0(\mathbf{r},t) + \mathbf{E}_i(\mathbf{r},t)$, where $\mathbf{E}_0(\mathbf{r},t)$ is the external field, as it propagates in vacuum, and $\mathbf{E}_i(\mathbf{r},t)$ is the field radiated by the accelerated charges in the target,

$$\mathbf{E}_i(\mathbf{r},t) = -\frac{1}{c^2}\int d\mathbf{r}'\frac{1}{|\mathbf{r}-\mathbf{r}'|}\left[\frac{\partial}{\partial t'}\mathbf{J}(\mathbf{r}',t')\right]_{t'=t-|\mathbf{r}-\mathbf{r}'|/c}. \tag{2}$$

Note that this expression assumes the generated radiation to propagate in vacuum. We see in the next subsection that this is a reasonable assumption for the high-order harmonics. For the fundamental field, we use a quasianalytical expression that takes into account the major contributions to the refractive index. Turning to a microscopic viewpoint, we decompose the target into a discrete sum of elementary contributions, associated with each charge in the sample. The transversal far field radiated by the jth charge, placed at point $\mathbf{r}_j$ in the target reads as

$$\mathbf{E}_i^j(\mathbf{r}_d,t) = \frac{1}{c^2}\frac{q_j}{|\mathbf{r}_d - \mathbf{r}_j(0)|}\mathbf{s}_d \times \{\mathbf{s}_d \times \mathbf{a}_j[t - |\mathbf{r}_d - \mathbf{r}_j(0)|/c]\} \tag{3}$$

where $\mathbf{a}_j$ is the charge's acceleration, evaluated at the retarded time, and $\mathbf{s}_d$ is the unitary vector pointing to a virtual detector located at $\mathbf{r}_d$. Note that we are using the dipole approximation, as the charge displacement during the interaction is assumed small in comparison to the wavelength of the radiation field (including its harmonics); therefore $\mathbf{r}_j(t) \simeq \mathbf{r}_j(0)$. This condition is easily attained in neutral gases as harmonics are generated by charges in the vicinity of the parent ion.

A. Main approximations

The exact evaluation of the charge displacement is a complex task, as their motion has to be computed self-consistently with the total field $\mathbf{E}(\mathbf{r},t)$. Therefore, some set of reasonable assumptions have to be used. In order to handle the problem properly, we split it into two basic processes: the generation of the field by the target radiators and the propagation of the complete field through the target.

1. Field generation

The field generation at the target is given by the charge accelerations at any instant of time. The accurate computation of this quantity requires a precise knowledge of the total field at the charge's location, including the incident laser field and the field generated at other locations of the sample. The influence of the harmonic field on the charge's dynamics is minimal, as the intensity of the harmonics is typically orders of magnitude below that of the fundamental field. Therefore, we may consider the charges driven solely by the influence of the fundamental field [10]. The generation of high-order harmonics requires a high-intensity external field that submits the matter charges to a nonperturbative interaction. The exact dynamics of the charge can only be computed by the numerical integration of the Schrödinger equation, which requires a substantial computing effort and becomes prohibitory for the evaluation of the general target response. A drastic simplification comes from the use of the strong-field approximation combined with S-matrix techniques. In our case, we use a recently developed method [13], here referred to as SFA+, to compute the single-charge response to the intense field. In comparison with other SFA methods, our approach retains the full quantum description of the dynamics and, yet, provides an integration procedure efficient enough to tackle the general problem of propagation (an outline of this method is presented in Sec. I B).

2. Field propagation

From the propagation viewpoint, the influence of the target on the field propagation can be categorized either by the changes in the field phase or by the field absorption. We derive now some quantitative estimations on the target influence for the fundamental field and high-order harmonics.

The target effect on the field phase can be described considering the contributions to the refractive index, associated with bound-bound, bound-free, or free-free transitions. For low-density media we may approximate

$$n \simeq 1 + 2\pi(\chi_{\mathrm{bb}} + \chi_{\mathrm{bf}} + \chi_{\mathrm{ff}}), \tag{4}$$

with χ_{ij} being the susceptibilities associated with each of the above contributions. Considering a characteristic propagation length L at the target, the phase effects induced during the propagation can be estimated by considering the change in the optical path associated with each process, $\Delta L_{ij} = L2\pi\chi_{ij}$. To establish some limit, we shall consider that a particular process is relevant if the associated change of the optical path is less than or equal to $1/10$ of the wavelength λ of the considered field (fundamental or harmonic). Therefore,

$$n_i L < \frac{\lambda}{20\pi}\frac{n_i}{\chi_{ij}}, \tag{5}$$

where n_i is the density of charges in the initial state of the transition.

Let us first consider the propagation of the field at the fundamental wavelength. In a typical experiment, it corresponds to the near infrared and, therefore, to photon energies well below the ionization threshold of, for instance, rare gases. The target response to the fundamental field is, therefore, dominated by the bound-bound transitions and by the potential contribution of the ionized electrons (free-free transitions). In the absence of resonances, we can estimate χ_{bb} according to the perturbative formula [17]

$$\chi_{\mathrm{bb}} \simeq \frac{n_b e^2}{m}\frac{f_{12}}{\omega_{12}^2 - \omega^2}, \tag{6}$$

where n_b is the density of atoms in the ground state, 1 labels the ground state, 2 the final level of the lowest energy transition, and f_{12} the oscillator strength. If we consider the $1s$-$2p$ transition of the hydrogen atom, $f_{12} = 0.1388$ [18], and the

wavelength of the Ti:sapphire laser ($\lambda = 800$ nm), Eq. (5) leads to the limiting condition

$$n_b L < 8.5 \times 10^{18}\text{cm}^{-2}. \tag{7}$$

In particular, for a typical density in low-pressure gases of 10^{18} cm^{-3}, the effect of the bound-bound transitions in the propagation of the fundamental field is small for propagation lengths below approximately 8 cm.

On the other hand, $\chi_{\text{ff}} = -\omega_p^2/\omega^2$, with $\omega_p^2 = n_f e^2/m$ and n_f being the density of free electrons. Therefore, the limiting condition for the fundamental field reads as

$$n_f L < 2.8 \times 10^{16}\text{cm}^{-2}. \tag{8}$$

For instance, assuming a 10% ionization during the pulse propagation, the effect of free charges in the propagation of the fundamental field for the previous example begins to be relevant at propagation lengths above approximately 2 mm. Therefore, free charges are the main cause of the phase effects in the propagation of the fundamental field.

Now let us consider the propagation of the qth-order harmonic. We assume that its frequency $q\omega$ is greater than the ionization potential; therefore the dominant processes are the bound-free and the free-free transitions. For the first type, the susceptibility can be derived from the perturbation theory as

$$\chi_{1f} \simeq \frac{\pi}{4\hbar} N_b |\mu_{1,\epsilon}|^2 D(\epsilon), \tag{9}$$

where ϵ is the energy of the final state in the continuum, $\epsilon = \epsilon_0 + \hbar\omega_0$ (ϵ_0 being the ground state energy and ω_0 the fundamental field frequency), $\mu_{1,\epsilon}$ is the electric dipole moment of the transition, and $D(\epsilon)$ is the density of states. For the case of hydrogen atoms, $\mu_{1,\epsilon}$ can be computed analytically if the continuum states are assimilated to plane waves. In this case, the angle-averaged squared dipole matrix element results in

$$|\mu_{1f}|^2 = \frac{8}{3\pi^2} m e^2 \frac{(2/a_0)^5}{\left[(1/a_0)^2 + 2m\epsilon\right]^6} \epsilon. \tag{10}$$

Under the assumption of a plane-wave continuum, the density of states $D(\epsilon)$ in Eq. (9) is given by the standard expression $(2m)^{3/2}\epsilon^{1/2}/2\pi^2\hbar^3$. A typical harmonic order near the spectrum cutoff for our laser parameters is 27th; so taking this as a reference the limit value (5) gives

$$n_b L < 2.6 \times 10^{20}\text{cm}^{-2}. \tag{11}$$

For the case of the free-free transitions, the susceptibility now reads as $\chi_{\text{ff}} = -\omega_p^2/q^2\omega_0^2$. For the 27th harmonic, we have

$$n_f L < 7.5 \times 10^{17}\text{cm}^{-2}. \tag{12}$$

Again the most relevant influence in the phase of the propagating harmonics comes from the free charges. For the typical case considered previously, the target length above which this process has to be taken into account is 7.5 cm. To describe the harmonics conforming the plateau structure in the spectrum, one should reduce this length to approximately 3 cm.

Second, let us evaluate the absorption loss during the propagation of a high-order harmonic. The absorption coefficient for the qth harmonic, α_q, can be evaluated from the ionization rate of the atoms Γ, as the fraction of photons absorbed per unit length,

$$\alpha = \frac{n_b \Gamma}{(I/\hbar\omega)}. \tag{13}$$

The ionization rate can be computed from the perturbation theory by Fermi's Golden Rule as $\Gamma = (4\pi^2/\hbar^2 c) I |\mu_{\text{bf}}|^2 g(\epsilon)$, with the same definitions as in Eq. (9). We define the limit for neglecting this process when the target length is 10 times smaller than the absorption depth, $L < 1/10\alpha$. For instance, for the 27th harmonic this gives the condition

$$n_b L < 5.3 \times 10^{18}\text{cm}^{-2}. \tag{14}$$

Again for the case of 10^{18} atoms/cm^3 gas, the limit length is approximately 5 cm and for the lower order harmonics of the plateau it is about 1.5 cm (assuming the matrix element as constant). Note that for high-order harmonics, the most relevant process influencing the propagation is photon absorption. Therefore, if condition (14) is fulfilled we can neglect the medium response and our starting formulation, Eq. (2), is well justified.

From the aforementioned considerations it becomes clear that the most relevant process is the presence of free charges in the medium, which affects especially the fundamental field. Even though for lengths smaller than the millimeter the change in optical path is small enough to be neglected, it still can have an important contribution for the phase matching of high-order harmonics. The wave number of the generated qth-order harmonic is, approximately, qk_1, while as we have seen the wave vector of the propagating harmonic field is approximately the vacuum $k_q = q\omega_0/c$. Therefore a small variation of the optical path of the fundamental field can be relevant for the emitted high-order harmonic. As before, we may consider this dephase not relevant if the change in optical path is smaller than 1/10 of the harmonic wavelength λ_0/q. Therefore the limit in the propagation distance is given by Eq. (8) divided by the harmonic order. For the 27th harmonic we have

$$n_f L < 1 \times 10^{15}\text{cm}^{-2}, \tag{15}$$

and, therefore, for the gas density considered above and 10% of free charges, this length is limited to 100 μm. This is a very restrictive condition, as interacting distances below hundreds of microns are not realistic at the laboratory.

Equations (8) and (15) point out the necessity of including plasma effects in the propagation of the fundamental field, if one wants to consider propagation lengths of the order of 1 cm. With the presence of free charges due to ionization, the wave number of the fundamental field is shifted from its vacuum value to $k_1^2 = k_0^2(1 - \omega_p^2/\omega_0^2)$, ω_p being the plasma frequency [16]. Taking into account that the gas jet is inhomogeneous, the spatial phase of the fundamental field at point $\mathbf{r}$ can be approximated by the integral over the propagation direction

$$\int_{-\infty}^{z} k_1(x,y,\xi) d\xi \simeq k_0 z - \frac{2\pi e^2}{\omega_0{}^2 m} P_f(\mathbf{r},t) \int_{-\infty}^{z} n(x,y,\xi)\, d\xi, \tag{16}$$

with $n(x,y,z)$ being the atomic density distribution and $P_f(\mathbf{r},t)$ the ratio for ionized electrons, which we calculate as follows

$$P_f(\mathbf{r},t) = 1 - e^{-\int_{-\infty}^{t} w_{\text{ADK}}(\mathbf{r},\tau)\, d\tau}, \tag{17}$$

where $w_{\mathrm{ADK}}(\mathbf{r},t)$ is the ionization rate, calculated from the Amosov-Delone-Krainov (ADK) equation [19]. For hydrogen this reads

$$w_{\mathrm{ADK}}(\mathbf{r},t) = \frac{2e^2}{\pi}\left[\frac{3}{\pi|E(\mathbf{r},t)|}\right]^{1/2} e^{-\frac{2}{3|E(\mathbf{r},t)|}}. \tag{18}$$

B. Evaluation of the source term

With the aforementioned approximations, the solution of Eq. (3) can be found by superposition of each target radiator, excited by the fundamental field $\mathbf{E}_1(\mathbf{r},t)$. For the case of intense fields the computation of the dynamics of the radiators is not trivial, as the interaction is nonperturbative. To this end, the exact numerical integration of the Schrödinger equation would be desirable. However, unless the field is approximated to a simple form (for instance a plane wave) or some additional assumptions are made [20], the necessity of such integration for each of the target radiators makes the whole problem unattainable. Therefore, the use of simplified models is almost mandatory. For the case of intense fields, S-matrix approaches combined with the strong-field approximation (SFA) offer a temporal approximated description of the problem. However, even within this framework, the resulting integral equations are traditionally considered to require long computations. As a further step, the saddle-point method is used to avoid multidimensional integrals in momentum space and time. The resulting model, which describes the process of harmonic generation in terms of semiclassical trajectories, offers a very transparent picture of the recollision process leading to high-order harmonic generation. During the last 15 years, this model has been employed extensively for the theoretical description of this process, as well as for the dynamical description of the source term in propagation. Despite its success, some recent results have pointed out the limitations of this model to reproduce quantitatively the harmonic spectra, failing, for instance, to describe the correct scaling of the highest-order harmonics with the wavelength [21]. The use of the saddle-point method, on the other hand, restricts the harmonic generation to the most relevant events (those described by the trajectories), while neglecting other processes leading to harmonic radiation (as the *way out* and *close up* contributions) which require a full quantum mechanical treatment [22]. In this context, we have recently developed a new method, alternative to the saddle point, which permits one to compute the harmonic spectrum including the complete momentum space and, yet, that can be computed with enough efficiency to be implemented in a propagation calculation. This new method also includes the influence of the field in the ground state during the recollision event that leads to harmonic generation. In this latter sense it represents an extension of the standard SFA, hence we refer it as SFA+. Although the detailed derivation of the SFA+ model can be found elsewhere [13], we sketch here the practical implementation of the model.

For simplicity, we assume that the target is composed of identical systems (atoms or molecules) initially in their ground state. In SFA+, the dipole acceleration at any instant of time is composed of two contributions:

$$a(t) = a_b(t) + a_d(t) + \mathrm{c.c.} \tag{19}$$

The first term, $a_b(t)$, stands for the dipole acceleration computed with the standard S-matrix SFA, but without resorting to the saddle-point method. The second term, $a_d(t)$, describes the correction introduced by the SFA+ model by including the relevant dynamics of the ground state during the recollision event leading to harmonic radiation. Within this approximation, the acceleration $a_b(t)$ is computed adding the contributions of each Volkov wave of the continuum, $a_b(t) = \int d\mathbf{k} a_b(\mathbf{k},t)$, with

$$a_b(\mathbf{k},t) = -\frac{i}{\hbar}C_F\int_{t_0}^{t} dt_1 e^{i\epsilon_0(t-t_1)/\hbar} e^{-i\frac{1}{\hbar}\int_{t_1}^{t}\epsilon(\mathbf{k},\tau)d\tau} \times \langle\phi_0|\hat{a}|\mathbf{k}\rangle V_i(\mathbf{k},t_1)\langle\mathbf{k}|r^{-1}|\phi_0\rangle, \tag{20}$$

where $V_i(\mathbf{k},t_1) = -(q/mc)A(t_1)k_z + q^2/(2mc^2)A^2(t_1)$, $\epsilon(\mathbf{k},\tau) = \hbar^2k^2/2m + V_i(\mathbf{k},\tau)$, and $A(t_1)$ is the potential vector of the linearly polarized driving field and $|\phi_0\rangle$ is the bound state with energy ϵ_0, initially occupied by the electron. We have introduced the Coulomb factor [23] for hydrogen $C_F/r = 2E_0/r$, with E_0 being the peak field amplitude. The acceleration operator is described as $\hat{a} = -(q/m)\partial V_c/\partial z$ (V_c being the atomic Coulomb potential, $-q^2/r$). For hydrogen, the matrix elements can be computed readily as

$$\langle\mathbf{k}|r^{-1}|\phi_0\rangle = \frac{\sqrt{2}}{\pi}\left(\frac{1}{a_0}\right)^{3/2}\frac{1}{(1/a_0)^2+k^2}, \tag{21}$$

$$\langle\phi_0|\hat{a}|\mathbf{k}\rangle = -\sqrt{2}i\frac{1q^2}{\pi m}\left(\frac{1}{a_0}\right)^{3/2}\frac{k_z}{k^2}\left[1-\frac{\arctan(ka_0)}{ka_0}\right]. \tag{22}$$

The numerical evaluation of $a_b(t)$ is usually considered demanding, since it implies an integral over the momentum space, and Eq. (20) requires also the evaluation of nested time integrals. In view of this, many authors resort to a saddle-point approximation. In our computations, however, we prefer to consider the differential version of Eq. (20),

$$\frac{d}{dt}a_b(\mathbf{k},t) = \frac{i}{\hbar}\left[\epsilon_0 - \epsilon(\mathbf{k},t)\right]a_b(\mathbf{k},t) - \frac{i}{\hbar}C_F\langle\phi_0|\hat{a}|\mathbf{k}\rangle V_i(\mathbf{k},t)\langle\mathbf{k}|r^{-1}|\phi_0\rangle. \tag{23}$$

This forms a set of uncoupled one-dimensional (1D) differential equations that can be solved numerically quite efficiently using a standard Runge-Kutta method. As the derivation of Eq. (23) from Eq. (20) does not involve any approximation, the evaluation of this latter equation gives the full information contained in the SFA S-matrix formulation (i.e., it includes complete information of the momentum space). By contrast, the use of the saddle-point approximation leads to a semiclassical description of harmonic generation.

The term $a_d(t)$ in Eq. (19) represents the correction of the SFA+ approach to the standard SFA, including the effect of the field on the bound state during the rescattering event. The rescattering takes place when a previously released electron is driven back to the parent ion by the intense field. The temporal lapse of the rescattering event, δt_s, is defined by the time during which the ground state wave packet and the free-electron wave packet overlap:

$$\delta t_s \simeq (3\pi/2\omega_0)\sqrt{|\epsilon_0|/3.17U_p}. \tag{24}$$

Assuming this is a small quantity in comparison with the laser field period, the time-dependent operators involved in the evaluation of $a_d(t)$ are approximated by their time averages over δt_s. After some steps, one can find the expression of the contribution of each momentum to a_d in terms of those for a_b,

$$a_d(\mathbf{k},t) = -\left[1 + \frac{k^2/2m - \epsilon_0}{\Delta_s}\right] a_b(\mathbf{k},t) \tag{25}$$

and $a_d(t) = \int d\mathbf{k} a_d(\mathbf{k},t)$. In this expression we define Δ_s as the average level shift during the rescattering, δt_s,

$$\Delta_s \simeq U_p + \frac{2\hbar}{\omega_0 \delta t_s}\sqrt{\frac{Up}{m}} k_z \sin(\omega_0 \delta t_s) + \frac{U_p}{2\omega_0 \delta t_s}\sin(2\omega_0 \delta t_s), \tag{26}$$

with

$$k_z = -\frac{2}{\hbar}\sqrt{mU_p}\frac{\sin\omega_0\delta t_s}{\omega_0 \delta t_s} \times\left[1 - \sqrt{1 - \frac{1}{6}\left(1 + \frac{\epsilon_0}{U_p} + \frac{\sin(2\omega_0\delta t_s)}{2\omega_0\delta t_s}\right)\left(\frac{\sin(\omega_0\delta t_s)}{\omega_0\delta t_s}\right)^{-2}}\right], \tag{27}$$

the averaged momentum in the direction of the field polarization, estimated from energy equipartition. The final form for the total acceleration is, therefore,

$$a(t) = -\int d\mathbf{k} \frac{\hbar^2 k^2/2m - \epsilon_0}{\Delta_s} a_b(\mathbf{k},t) + \text{c.c.}, \tag{28}$$

with $a_b(\mathbf{k},t)$ computed numerically from Eq. (23). The target-induced field, in Eq. (3), is computed evaluating Eq. (28) for every target radiator.

The quantitative accuracy in the evaluation of the source term is a fundamental requirement for a faithful computation of the harmonic propagation. In Fig. 1 we show a comparison between the spectra of the dipole acceleration resulting from the exact numerical solution of the two-dimensional Schrödinger equation (TDSE) and our SFA+ model. The laser field corresponds to the focal point of the Gaussian beam considered in the next section (intensity $\simeq 1.58 \times 10^{14}$ W/cm^2 and 800-nm wavelength) and the atomic species is hydrogen. The plots in the figure correspond to the direct outcome from the Fourier transform of the dipole acceleration in the different approaches; that is, no relative shift or scalings have been used. The result of the exact computation of the three-dimensional (3D) TDSE is plotted with the green line, while the result of the SFA+ computation is plotted with the red line. We can see that the agreement between both calculations is quantitatively good for the high-order harmonics (above the 21st). For the lower frequencies, the progressive departure of the model's results in comparison with the exact TDSE reflects the limitation of the SFA, as it neglects the contributions of the atomic excited states. The accuracy of the phase description of the radiated spectrum is found to be very similar with SFA+ as well as with the standard SFA, and reasonably good in comparison with the exact TDSE [24].

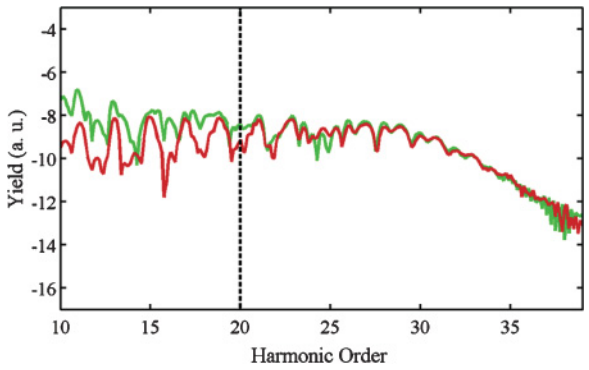

FIG. 1. (Color online) Comparison of the single-atom harmonic spectra computed from the exact numerical integration of the TDSE [green (light gray) line] and the SFA+ model [red (dark gray) line] for an eight-cycle pulse of $\sin^2$ shape, with intensity $\simeq 1.57 \times 10^{14}$ W/cm^2 and a wavelength of 800 nm. The calculations are carried out for hydrogen.

Note that, although the atomic species considered in this article is hydrogen, the aforementioned formalism is equally applicable to other cases replacing the corresponding matrix elements and Coulomb factor, as long as the single active approximation is valid. The determination of these parameters in other rare gases, and the corresponding test of our model with the exact TDSE solutions, is currently under way.

C. Discrete dipole approximation

For low-pressure densities of 10^{18} atoms/cm^3, the number of target radiators in a typical interaction region is of the order of 10^{12}. This means that, despite the use of efficient models for the computation of the source term, the computation of the dynamics of each dipole required by Eq. (2) becomes a formidable task. To overcome this limitation we use the DDA [11,12], where the interaction volume is split into discrete cells, each containing a macroscopic number of radiators. The computation of the source term is therefore simplified if the following conditions are met:

(i) The number of dipoles enclosed in each cell is large enough to approximate their density by a continuous distribution. We shall then define a lower limit for the cell's size to enclose about 10 dipoles in each dimension, that is, $d > 10[1/n(\mathbf{r}_j)]^{1/3}$, d being the cell's diameter, $n(\mathbf{r}_j)$ the atom density, and $\mathbf{r}_j$ the coordinate of the cell's center. For the aforementioned gas density, this lower limit is about 100 nm. To avoid parasitic diffraction we skip the definition of sharp edges at the cell limits, replacing the geometrical shape of the cell by a localized Gaussian distribution of the same width $n(\mathbf{r}_j)V_{\text{cell}}g(\mathbf{r}')$ (V_{cell} being the cell's volume), with

$$g(r') = Ce^{-r'^2/\sigma^2}, \tag{29}$$

where C is the normalization factor, σ is related to the diameter of the sphere d as $d = 2\sigma\sqrt{\ln 2}$, and $\mathbf{r}'$ is a coordinate on the local reference frame with origin O' at the cell's center $\mathbf{r}_j$ (see Fig. 2).

(ii) The size of the cells is small enough to approximate the external field as a local plane wave with a uniform intensity distribution within the cell's volume. Denoting W_0 as a characteristic length for the variation of the intensity distribution of the external field, we shall define the upper limit of the cell's diameter as $d < 2W_0/10$. For the numerical results presented in this article, we consider a Gaussian beam

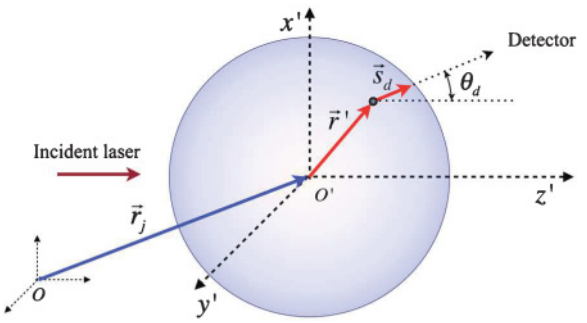

FIG. 2. (Color online) Scheme of the finite-size cell considered to apply the DDA. The direction of the detector is defined by the vector $\mathbf{s}_d$. The local reference frame has its origin O' at the cell's center, $\mathbf{r}_j$, and it is oriented so that the z' axis coincides with the propagation direction of the local plane-wave field, and $\mathbf{s}_d$ has no y' component.

(see Sec. II) whose beam waist is $W_0 = 30$ and, therefore, the cell's diameter d should not exceed 6 μm.

(iii) The total number of cells is determined by the ratio between the interaction region and the cell's volume: $N_c \simeq V_{\text{int}}/V_{\text{cell}}$. In the practical case, however, the choice of the cell's location is determined by a Monte Carlo method from the target density distribution. Therefore, the computation can finish according to a convergence criteria, before scanning the total number of cells.

If the previous conditions are met, the radiators within a cell interact approximately with the same form of the external field. Consequently, denoting $\mathbf{E}_1(\mathbf{r}_j,t)$ the fundamental field as seen at the center of cell j, the interacting field at any neighbor point $\mathbf{r}'$ can be approximated by $\mathbf{E}_1(\mathbf{r}_j,t_{\mathbf{r}'})$, with $t_{\mathbf{r}'}$ being the temporal lag associated with the distance of this point to O'. The z' axis being the propagation direction of the local plane-wave field, $t_{\mathbf{r}'} = t - z'/c$. Therefore, according to Eq. (3), the total field at the detector position $\mathbf{r}_d$ emitted by a single cell is given by

$$\mathbf{E}_{i,j}(\mathbf{r}_d,t) \simeq \frac{N(\mathbf{r}_j)}{c^2|\mathbf{r}_d|}\int d\mathbf{r}' g(\mathbf{r}')\mathbf{s}_d \times\left[\mathbf{s}_d \times \mathbf{a}\left(\mathbf{r}_j, t - \frac{z'}{c} - \frac{|\mathbf{r}_d - \mathbf{r}' - \mathbf{r}_j|}{c}\right)\right], \quad (30)$$

where $\mathbf{a}(\mathbf{r}_j,t)$ is the dipole acceleration computed with Eq. (28), induced by the response to the fundamental field. For the case of isotropic radiators, the direction of the vector $\mathbf{a}(\mathbf{r}_j,t)$ is the driving field's polarization. $\mathbf{r}_d$ is the detector's coordinate, which is assumed to be at an arbitrarily large distance from the interaction region, $|\mathbf{r}_d| >> |\mathbf{r}_j|$ (see Fig. 3).

Equation (30) can be integrated in the time-frequency domain,

$$\mathbf{E}_{i,j}(\mathbf{r}_d,\omega) \simeq \frac{N(\mathbf{r}_j)}{c^2|\mathbf{r}_d|}\int d\mathbf{r}' g(\mathbf{r}')\mathbf{s}_d \times\left[\mathbf{s}_d \times \mathbf{a}(\mathbf{r}_j,\omega) e^{i\omega\left(\frac{z'}{c} + \frac{|\mathbf{r}_d - \mathbf{r}' - \mathbf{r}_j|}{c}\right)}\right], \quad (31)$$

dropping constant terms, we have

$$\mathbf{E}_{i,j}(\mathbf{r}_d,t) \propto N(\mathbf{r}_j)\mathbf{s}_d \times\left[\mathbf{s}_d \times \mathbf{a}(\mathbf{r}_j,\omega) e^{-i\omega\frac{|\mathbf{r}_d - \mathbf{r}_j|}{c}} F(\theta_{d,j},\omega)\right], \quad (32)$$

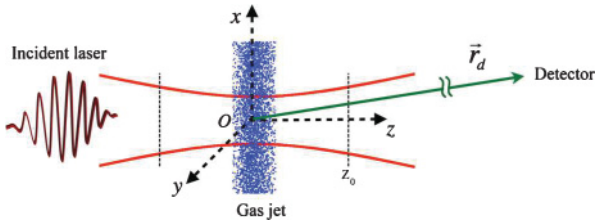

FIG. 3. (Color online) Scheme of the high-order harmonic experiment considered in this article: An eight-cycle Gaussian pulse is focused near the center of a gas jet. The peak intensity at the focus is 1.57×10^{14} W/cm^2, the wavelength is 800 nm, and the waist is 30 μm. The gas jet has a constant profile in the x direction and a Gaussian profile in the y and z directions, with widths of 500 μm and a peak density of 10^{18} atoms/cm^3. The coordinate origin, O, is located at the laser focus and the jet position is translated along the z axis.

where $F(\theta_{d,j},\omega)$ is a form factor defined as

$$F(\theta_{d,j},\omega) = \lim_{|\mathbf{r_d}|\to\infty}\int d\mathbf{r}' g(\mathbf{r}') e^{i\omega\left(\frac{z'}{c} - \frac{|\mathbf{r}_d - \mathbf{r}' - \mathbf{r}_j|}{c} + \frac{|\mathbf{r}_d - \mathbf{r}_j|}{c}\right)} = \int d\mathbf{r}' g(\mathbf{r}') e^{i\frac{\omega}{c}(z' - \mathbf{s}_d\cdot\mathbf{r}')}, \quad (33)$$

where $\mathbf{s}_d$ is the unitary vector pointing to the detector direction and $\mathbf{s}_d = cos\theta_{d,j}\mathbf{e}_{z'}$, according to the chosen orientation of the local reference frame (Fig. 2). Using Eq. (29), the integral can be evaluated analytically as

$$F(\theta_{d,j},\omega) \propto e^{\frac{1}{2}\frac{\omega^2}{c^2}\sigma^2(1-\cos\theta_{d,j})}, \quad (34)$$

with $\theta_{d,j}$ being the angle between the detector position and the local-field propagation vector at the cell j. Note that Eq. (32) corresponds to the field of a single radiator located at the cell's center $\mathbf{r}_j$, modulated by a form factor $F(\theta_{d,j},\omega)$ that takes into account the interfering contributions of the rest of the radiators in the macroscopic cell. Figure 4 shows the angular distribution of the high-order harmonic radiated spectra in linear scale (a) for a single radiator and for cells of diameters (b) 10 nm, (c) 50 nm, and (d) 500 nm. Note that, as a result of the macroscopic size of the cell, the global matching of the field emitted by the different points in the cell leads to a constructive interference restricted near the propagation direction of the fundamental field.

II. RESULTS

Let us now present some results of our calculation for the model experiment depicted in Fig. 3. We first introduce the mathematical definitions of the field and the gas jet distributions and then characterize the convergence of the model. We then study the different phase contributions to the macroscopic harmonic spectrum and analyze the phase-matching conditions at different target positions.

For the results presented in this article, we have considered a low-pressure hydrogen jet interacting with an 800-nm laser pulse of eight cycles with a peak intensity of 1.57×10^{14} W/cm^2. For the description of the laser pulse, we have considered a Gaussian beam, so the fundamental field

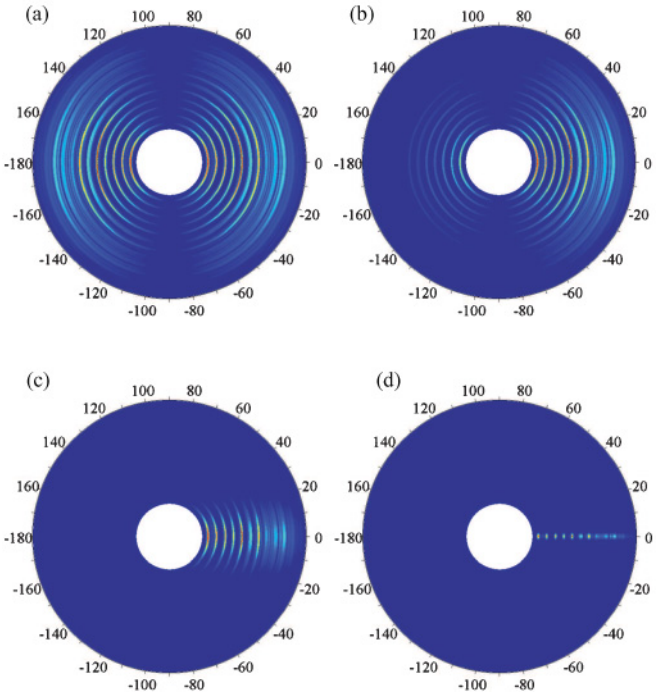

FIG. 4. (Color online) Angular distribution of the radiation spectra, in linear scale, (a) for a single radiator and cells (b) 10 nm, (c) 50 nm, and (d) 500 nm in diameter. The radial axis corresponds to the harmonic order (starting at the 21st), angles are represented in degrees and the z axis is parallel to the propagation direction of the local plane wave.

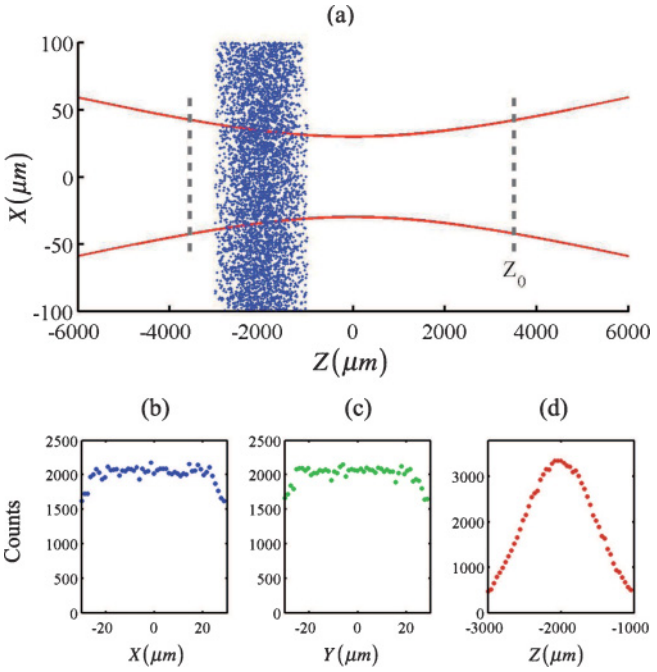

FIG. 5. (Color online) Distribution of atoms in the gas jet, corresponding to Eq. (37) with the following parameters: $y_c = 0$, $z_c = -2$ mm, $\sigma_y = 500$ μm, and $\sigma_z = 500$ μm. In (a) we plot the x-z distribution, while in (b) to (d) we plot the distributions corresponding to each dimension. The beam waist is $W_0 = 30$ μm and the Rayleigh range, marked with the dashed line in (a), results in $z_0 = 3.5$ mm.

has the form

$$\mathbf{E}_1(\mathbf{r},t) = E_0\eta(z-ct)U(\mathbf{r})e^{-i\left(\int_{-\infty}^{z} k_1(x,y,\xi)d\xi-\omega_0 t\right)}, \quad (35)$$

where E_0 is the peak field amplitude, $\eta(z-ct)$ is a $\sin^2$ temporal envelope, eight cycles long, and $U(\mathbf{r})$ is a Gaussian profile, whose expression is

$$U(\mathbf{r}) = \frac{W_0}{W(z)} e^{-\frac{\rho^2}{W^2(z)}} e^{i\frac{\omega}{c}\frac{\rho^2}{2R(z)}+i\zeta(z)}, \quad (36)$$

where $W(z) = W_0\sqrt{1+(z/z_0)^2}$ is the expression for the beam width, where W_0 is the beam waist, related to the Rayleigh range (z_0) as $W_0 = \sqrt{\lambda z_0/\pi}$, $R(z)$ is the wavefront radius of curvature, given by $R(z) = z[1+(z_0/z)^2]$, and $\zeta(z)$ is the Gouy phase, which is given by $\zeta(z) = \tan^{-1}(z/z_0)$. In the results presented in this article, the beam waist is $W_0 = 30\,\mu$m, and hence the Rayleigh range is $z_0 = 3.5$ mm. In the following, we define $z = 0$ as the position of the focus along the propagation axis z. The spatial integral in the exponent of Eq. (35) is computed using Eq. (16). On the other hand, the gas jet, directed along the x axis (perpendicular to the field propagation), is modeled by a Gaussian distribution along the y and z dimensions and by a constant profile along its axial dimension, x. Therefore, the atom-density distribution is given by

$$n(y,z) = n_0 e^{-\frac{(y-y_c)^2}{2\sigma_y^2}} e^{-\frac{(z-z_c)^2}{2\sigma_z^2}}, \quad (37)$$

where n_0 is the maximum gas density over the interacting volume, and y_c and z_c are the coordinates of the beam axis center with respect to the laser-beam focal point (located at the origin). The quantities σ_y and σ_z are the half width half maximum of the Gaussian distribution in each direction, respectively. Figure 5 shows the particular example where the gas jet is placed 2 mm before the focus of the beam (i.e., $z_c = -2$ mm), with $\sigma_z = 500$ μm. In the transversal direction, the parameters of the Gaussian distribution are $y_c = 0$ μm and $\sigma_y = 500$ μm.

A. Convergence of the model

As we stated in Sec. IC, for the particular example considered here, the diameter of the discrete cells must be enclosed in the interval 100 nm $< d <$ 6 μm. Although the final result is independent on the actual choice within this interval, the use of smaller diameters dilates the computing time, as the same convergence goal is attained computing a larger number of cells. This is illustrated in Fig. 6 where we present results for three different diameters. For better comparison, the first column shows the results of the bare problem, that is, a collection of point dipoles, while columns 2 to 4 present the results of the DDA computations using cells with diameters of 1, 2, and 3 μm, respectively. The convergence of each case is illustrated through the different rows, which correspond to a different number of cells. Note that for 10^5 cells (6th row) all cases have converged, including the bare case. On the other hand, it becomes evident that using cells of larger diameter reduces the convergence time. In particular, for the choice of 3 μm it is sufficient to consider 10^4 cells to obtain good results, which means a reduction of computing time of 1 order of magnitude in comparison with the bare dipole case.

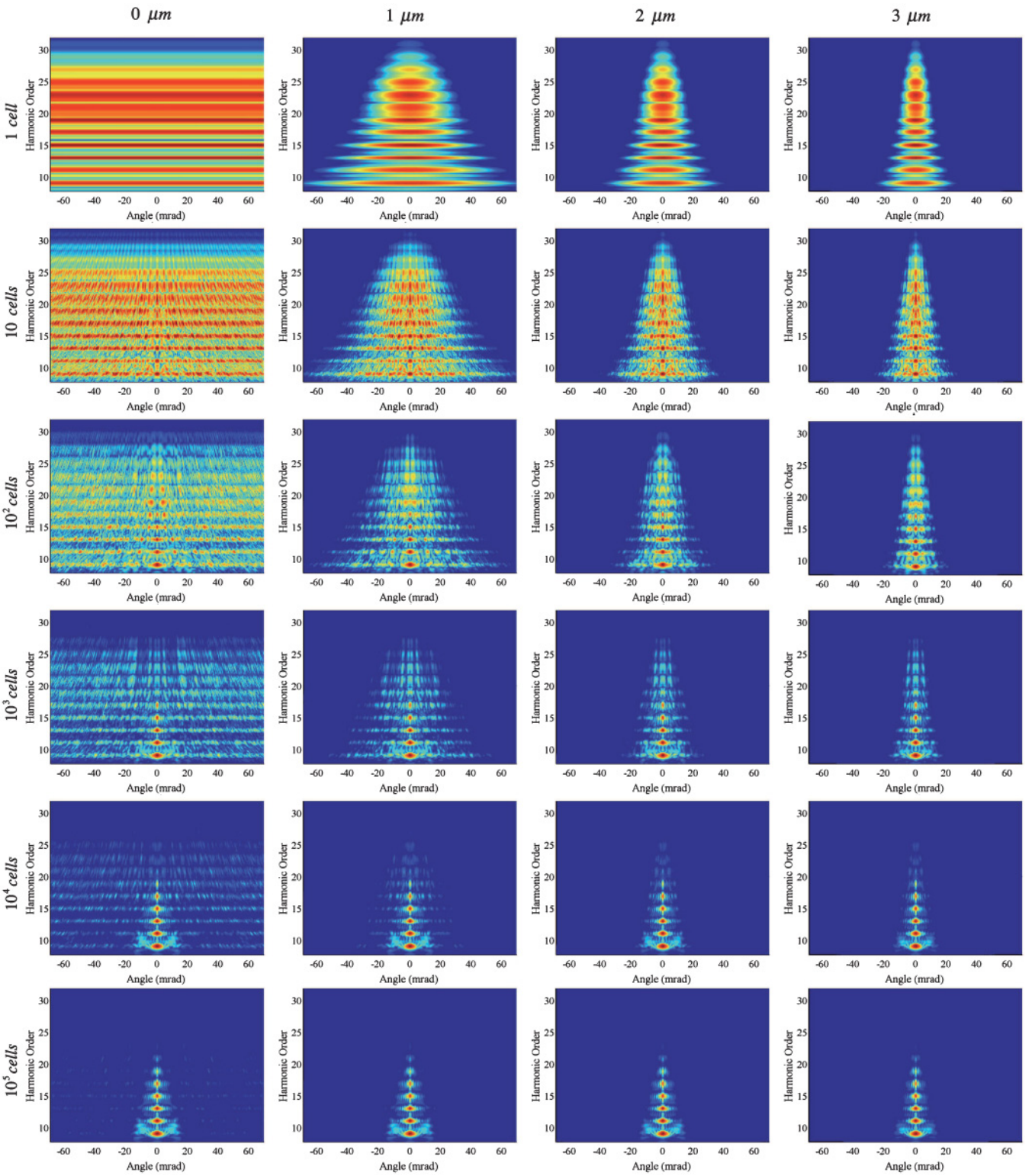

FIG. 6. (Color online) Angle-resolved high-order harmonic spectra for different number and size of spheres within the DDA. in the column on the left, the simulation is done without the DDA approximation, that is, considering pure atoms. In the others columns, from left to right we have 1-, 2-, and 3-μm-diameter spheres. However, in the first row we have 1 sphere, while 10, 10^2, 10^3, 10^4, and 10^5 spheres are considered in the following ones. The gas jet is placed 1 mm before the focus of the laser beam. The laser pulse is eight cycles 800 nm with a peak intensity of 1.57×10^{14} W/cm^2.

B. Phase matching along the propagation axis

The phase of the high-order harmonics has three different contributions: (i) one due to the Gouy phase associated with the Gaussian laser beam, whose expression is $q\zeta(z)$, q being the order of the harmonic; (ii) the intrinsic phase, which depends mainly on intensity and is a consequence of the rescattering

mechanism for harmonic generation in the single atom; and (iii) the dephase produced in the fundamental field by the presence of free electrons, which is imprinted to the harmonics as a result of the nonlinear process of harmonic generation. As discussed before, this later contribution becomes especially important for propagation lengths of the order of a few millimeters or even below, and if the gas jet is placed close to the focus of the beam where the intensity is maximum.

Our method allows one to naturally isolate the contributions of the different target points to the harmonic spectrum and, also, to separate the different physical contributions to the total phase of the harmonics. In Fig. 7 we have plotted the phase of harmonic 21 in two different situations. In Fig. 7(a) the gas jet is placed 2 mm before focus, while in Fig. 7(b) it is placed 2 mm after the focus. In both figures we have represented the different contributions to the phase: dashed red, the Gouy phase; dotted pink, the intrinsic phase; dashed-dotted green line, the sum of the Gouy and the intrinsic phase; and solid blue line, the total phase, including also ionization. Figures 7(c) and 7(d) correspond to the derivative of the total phase along the propagation length, corresponding to Figs. 7(a) and 7(b), respectively. In the background, the light grey line represents the atom distribution along the propagation axis.

The comparison of Figs. 7(a) and 7(b) shows that, while the Gouy phase always decreases with the distance, the slope of the intrinsic phase, which depends on the intensity gradient, is antisymmetric with respect to the laser focal point. Therefore, when the gas jet is located before the focus, the intrinsic phase decreases with z, while when located after the beam focus it increases. This is a fundamental difference, as in this latter case the opposite behavior of the intrinsic and Gouy phase compensates and results in a nearly flat phase distribution (Fig. 7(b), dashed-dotted green line) in the region $z > 2.5$ mm. The addition of the dephase induced by free charges leads to a total phase (solid blue line) of equal characteristics. On the other hand, if the target is located before the focus, both intrinsic and Guoy phases increase, adding up to a total phase which varies rapidly with z [green line, Fig. 7(a)]. Moreover, the dephase induced by free charges now has a stronger contribution, increasing further the spatial variation of the total phase (blue line). Figures 7(c) and 7(d) show the derivative of the total phase along the z axis, where we can see that the minimal variation of the phase corresponds to the gas jet positioned after the focus.

In high-order harmonic propagation, phase-matching conditions strongly affect the signal arriving at the detectors. This signal is optimal if the radiation emitted by an atom interferes constructively with the others. Therefore, the most

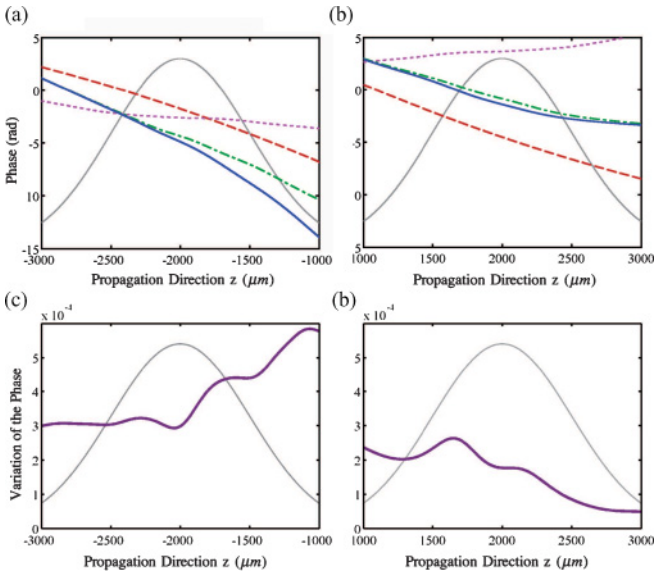

FIG. 7. (Color online) Spatial distribution of the phase of the 21st harmonic along the propagation axis z when the gas jet is placed (a) before the focus position, $z_c = -2$ mm, and (b) after the focus position, $z_c = 2$ mm. The different contributions to the phase are plotted as follows: dashed red line, the Gouy phase; dotted pink line, the intrinsic phase; dashed-dotted green line, the sum of the Gouy and the intrinsic phase; and solid blue line, the total phase, including also ionization. Panels (c) and (d) represent the phase derivative of 21st harmonic along the propagation axis z when the gas jet is placed 2 mm before and after the focus, respectively (solid purple line). In the background of all the figures, the light grey line represents the gas jet profile along the propagation axis.

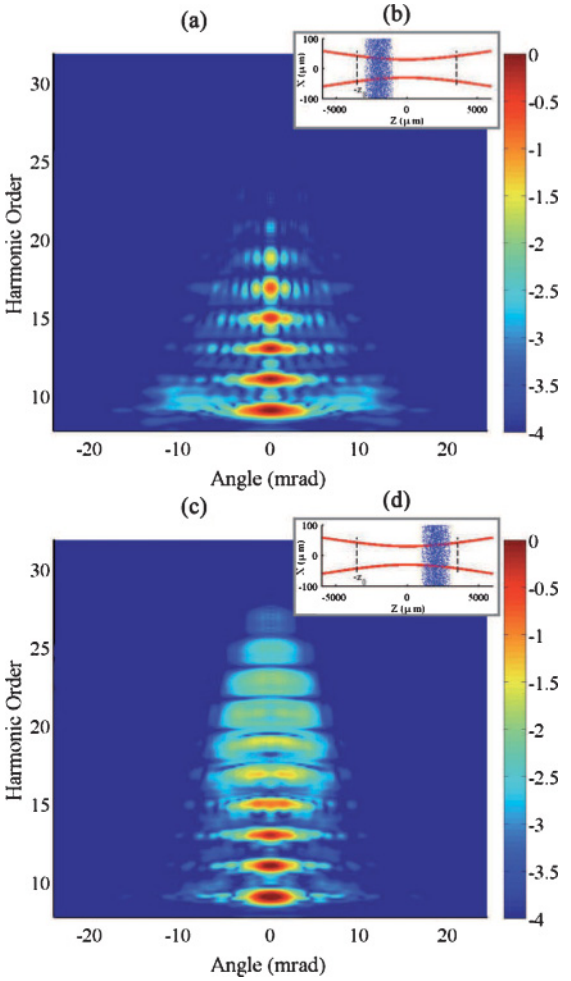

FIG. 8. (Color online) Angle-resolved high-order harmonic spectra when the gas jet was placed 2 mm (a) before and (c) after the focus of the laser beam. In panels (b) and (d) we can see the position of the gas jet and the laser beam in both situations, respectively. The laser pulse was eight cycles @ 800 nm with a peak intensity of 1.57×10^{14} W/cm^2 and a beam waist of 30 μm.

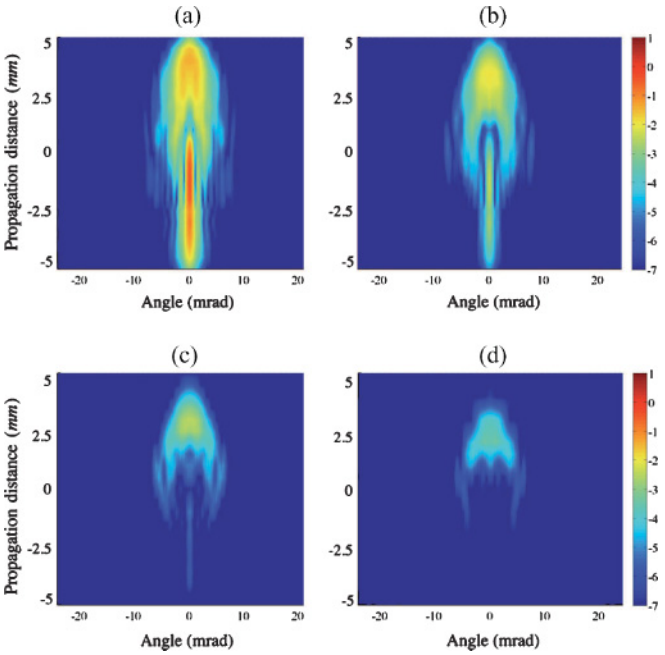

FIG. 9. (Color online) Spatial profile of high-order harmonics: (a) 17th, (b) 19th, (c) 21st, and (d) 23rd, when the gas jet is placed in different positions relative to the focus position, along the propagation axis.

relevant contribution to the macroscopic radiation comes from the target regions where the phase variation of the emitted harmonic in space is minimal [25]. Figure 8 shows the angle-resolved high-order harmonic spectra when the gas jet is placed 2 mm (a) before and (c) after the focus. In correspondence with the preceding discussion, we can observe an enhancement of high-order harmonics when the gas jet is placed after the focus. In addition we can observe some rings appearing in the harmonics profile when the laser is focused after the gas jet. These structures reflect the rapid change of the phase-matching conditions with the angle, as explained in Ref. [26]. These profiles are in excellent agreement with the results presented in Refs. [14,15,20].

Another issue that we can observe in Fig. 8 is the reduction of the cutoff frequency due to propagation. The theoretical value for the maximum emitted frequency in high-harmonic generation corresponds to $I_p + \kappa U_p$ with $\kappa = 3.17$ [27]. In hydrogen, with the parameters of our simulation, this corresponds to the 28th harmonic (see Fig. 1). Nevertheless, in Fig. 8 we can observe that the maximum harmonic is below the 28th harmonic and near the 21st harmonic. This value will correspond to $\kappa \simeq 2$, which is in good agreement with those observed in Ref. [28].

Finally, we show in Fig. 9 the variation of the angular profile of a particular harmonic when the position of the gas jet is varied continuously along the propagation axis. The variation of the angular profile is represented for the following harmonics: (a) 17th, (b) 19th, (c) 21st, and (d) 23rd. As discussed previously, the ring structures appear for target positions before or at the focus, while after the focus the angular structure becomes smoother. The figure also describes the variations of the intensity of the radiated harmonics with the location of the target. As we can observe, the higher the harmonic is, the more contrast exists between the signal of the harmonic before and after the focus. While in the 17th harmonic this difference is not very important, as we increase the order of the harmonic, it becomes critical, as for example in the 23rd harmonic, where there is no signal before the focus.

III. CONCLUSION

We have developed an approach for computing high-order harmonic propagation using the DDA. Our model is based on the S-matrix SFA + theory for the computation of the single-atom harmonic generation. The macroscopic response is computed from the superposition of the single-atom emission at the different points of the target and, thus, avoids the numerical integration of the wave equations. We have shown the feasibility of our approach by analyzing a typical experiment of harmonic generation with low-pressure gases, where we have studied the dependence of the harmonic emission with the target's position and compared our results with the existing data in the literature.

ACKNOWLEDGMENTS

We acknowledge support from Spanish Ministerio de Ciencia e Innovación through the Consolider Program SAUUL (CSD2007-00013) and Research Project FIS2009-09522, from Junta de Castilla y León through the Program for Groups of Excellence (GR27), and from the EC's Seventh Framework Programme (LASERLAB-EUROPE, Grant No. 228334). We also acknowledge support from the Centro de Laseres Pulsados, CLPU, Salamanca, Spain.

[1] K. J. Schafer, B. Yang, L. F. DiMauro, and K. C. Kulander, Phys. Rev. Lett. **70**, 1599 (1993).
[2] P. B. Corkum, Phys. Rev. Lett. **71**, 1994 (1993).
[3] Ch. Spielmann *et al.*, Science **278**, 661 (1997).
[4] Z. Chang, A. Rundquist, H. Wang, M. M. Murnane, and H. C. Kapteyn, Phys. Rev. Lett. **79**, 2967 (1997).
[5] E. Mével *et al.*, in *Ultrafast Phenomena XV* (Springer, New York, 2007), Springer Series in Chemical Physics.
[6] A. Zaïr *et al.*, Phys. Rev. Lett. **100**, 143902 (2008).
[7] M. Lein, J. Phys. B **40**, R135 (2007).
[8] J. Marangos *et al.* in *Strong Field Physics* (Springer, New York, 2008).
[9] A. L'Huillier *et al.*, J. Opt. Soc. Am. B **7**, 527 (1990).
[10] A. L'Huillier, P. Balcou, S. Candel, K. J. Schafer, and K. C. Kulander, Phys. Rev. A **46**, 2778 (1992).
[11] E. M. Purcell and C. R. Pennypacker, Astrophys. J. **186**, 705 (1973).

[12] M. A. Yurkin and A. G. Hoekstra, J. Quant. Spectrosc. Radiat. Transfer **106**, 558 (2007).
[13] J. A. Pérez-Hernández, L. Roso, and L. Plaja, Opt. Express **17**, 9891 (2009).
[14] P. Salières, Anne L'Huillier, and M. Lewenstein, Phys. Rev. Lett. **74**, 3776 (1995).
[15] J. Peatross, M. V. Fedorov, and K. C. Kulander, J. Opt. Soc. Am. B **12**, 863 (1995).
[16] J. D. Jackson, *Classical Electrodynamics* (Wiley & Sons, New York, 1999).
[17] B. W. Shore, *The Theory of Coherent Atomic Excitation* (Wiley & Sons, New York, 1990)
[18] [http://physics.nist.gov/PhysRefData/ASD/lines_form.html].
[19] M. V. Amosov, N. B. Delone, and V. P. Krainov, Zh. Eksp. Teor. Fiz. **91**, 2008 (1986) [Sov. Phys. JETP **64**, 1191 (1986)].
[20] M. B. Gaarde, Ph. Antoine, A. L'Huillier, K. J. Schafer, and K. C. Kulander, Phys. Rev. A **57**, 4553 (1998).
[21] J. Tate, T. Auguste, H. G. Muller, P. Salières, P. Agostini, and L. F. Di Mauro, Phys. Rev. Lett. **98**, 013901-1-4 (2007).
[22] J. A. Pérez-Hernández and L. Plaja, Phys. Rev. A **76**, 023829 (2007).
[23] V. P. Krainov, J. Opt. Soc. Am. B **14**, 425 (1997).
[24] J. A. Pérez-Hernández, J. Ramos, L. Roso, and L. Plaja, Laser Phys. **20**, 1044 (2010).
[25] V. Yakovlev, M. Ivanov, and F. Krausz, Opt. Express **15**, 15351 (2007).
[26] P. Balcou, P. Salières, Anne L'Huillier, and M. Lewenstein, Phys. Rev. A **55**, 3204 (1997).
[27] J. L. Krause, K. J. Schafer, and K. C. Kulander, Phys. Rev. Lett. **68**, 3535 (1992).
[28] A. L'Huillier, M. Lewenstein, P. Salieres, P. Balcou, M. Y. Ivanov, J. Larsson, and C. G. Wahlstrom, Phys. Rev. A **48**, R3433 (1993).